JOURNAL OF PROPULSION AND POWER
Vol. 16, No. 2, March–April 2000

Pulse Detonation Magnetohydrodynamic Power

Ron J. Litchford,* Bryan R. Thompson,† and John T. Lineberry‡
ERC Incorporated, Tullahoma, Tennessee 37388

A series of laboratory-scale experiments were conducted to investigate the basic engineering performance characteristics of a pulse detonation-driven magnetohydrodynamic electric power generator. In these experiments, stoichiometric oxy-acetylene mixtures seeded with a cesium–hydroxide/methanol spray were detonated at atmospheric pressure in a 1-m-long tube having an i.d. of 2.54 cm. Experiments with a plasma diagnostic channel attached to the end of the tube confirmed the attainment of detonation conditions ($p_2/p_1 \sim 34$ and $D \sim 2400$ m/s) and enabled the measurement of current density (~ 2 A/cm^2) and electrical conductivity (~ 6 mho/m) behind the detonation wave front. In a second set of experiments, a 30-cm-long continuous electrode Faraday channel, having a height of 2.54 cm and a width of 2.0 cm, was attached to the end of the tube using an area transition duct. The Faraday channel was placed inside a permanent magnet assembly having a nominal magnetic induction of 0.6 T, and the electrodes were connected to an active loading circuit to characterize power-extraction dependence on load impedance while also simulating higher effective magnetic induction. The experiments indicated peak power extraction at a load impedance between 5 and 10 Ω. The measured peak electrical energy density ranged from 10 to 10^3 J/m^3 when the effective magnetic induction was varied from 0.6 to 4.2 T. These results were in reasonable agreement with a simple electrodynamic model incorporating a correction for near-electrode potential losses. By scaling-up to a practical-size device, limiting the near-electrode potential drop to 10% of the induced potential, and optimizing seed-atomization characteristics, we anticipate a five- to tenfold increase in attainable electrical energy density.

Nomenclature

A = cross-sectional area
B = magnetic induction or flux density
C = capacitance
c = chord of cylinder cross section
D = detonation wave speed
d = distance between probe electrodes
E = electric field
f = Lorentz body force
H = magnetic field or intensity
h = channel height
i = current
j = current density
K = load factor
L = channel length
$\mathcal{L}$ = inductance
$\mathcal{P}$ = power density
p = pressure
q = electric charge
R = resistance
R_h = magnetic force number
R_m = magnetic Reynolds number
S = magnetic interaction parameter
T = temperature
t = time/electrode thickness
u = velocity
V = terminal load voltage
v = voltage
W = energy
w = channel width/electron drift velocity
x = coordinate axis
y = coordinate axis
Δ = dimensionless voltage drop
δ = slug thickness
ε = electromotive force
ζ = radial coordinate
Λ = line source strength
ξ = efficiency coefficient
σ = electrical conductivity
ϕ = electric potential

Subscripts

app = applied condition
b = burned gas condition
D = detonation
d = lump loss parameter
dif = difference value
e = electrical characteristic
eff = effective value
es = equipotential surface
i = internal parameter
ign = ignition condition
ind = induced parameter
max = maximum value
oc = open circuit
p = push work
0 = original or characteristic condition
1 = condition before detonation
2 = condition after detonation

Received 4 June 1998; revision received 20 December 1998; accepted for publication 21 December 1998.

*Project Manager, Advanced Development Projects; currently, Research Scientist, Propulsion Laboratory, NASA Marshall Space Flight Center, Huntsville, AL 35812. Senior Member AIAA.
†Engineer, Research and Product Development Division. Member AIAA.
‡Vice President, Research and Product Development Division. Senior Member AIAA.

Introduction

BECAUSE of intense technology development efforts, pulse detonation engines (PDE) are rapidly becoming an attractive low-cost alternative to gas-turbine engines for specialized propulsion and power applications. The practical advantages of PDEs are derived primarily from their improved thermodynamic efficiency (constant volume Humphrey cycle) and relative design simplicity (no turbomachinery). For example, the combustion detonation wave is associated with thermodynamic features that lend themselves to

high-power density engine designs. Furthermore, PDEs do not require high levels of precompression, and flow-path turbomachinery can be reduced or eliminated such that the compression, combustion, and thrust-generating processes are consolidated within a single component, thereby yielding a high thrust-to-weight ratio, relative design simplicity, and enhanced reliability.

The feasibility of the basic PDE concept has been proven in several experimental and theoretical studies as noted in recently published review articles.[1,2] However, there are certain developmental issues affecting the application of PDEs that have yet to be fully resolved.[3] Assuming that these development issues can be successfully addressed, we are currently investigating the opportunity for direct electric power production using the detonation combustion wave to drive a magnetohydrodynamic (MHD) generator. This concept is closely associated with explosive-driven MHD pulse power generators and high-temperature current layer (T-layer) MHD devices with which the authors have previous experience.[4,5] The rationale for integrating an MHD generator with a PDE was derived from a consideration of electric power requirements for normal engine operation, e.g., direct detonation initiation, and from anticipated needs for airborne auxiliary/burst power.

The authors are aware that a detonation-driven MHD generator can only convert the kinetic energy of the combustion products into electrical power. Thus, the enthalpy extraction efficiency of such a device will not be comparable with a typical generator configuration utilizing thermal combustion conditions and a flow-accelerating nozzle. Nevertheless, the detonation-driven MHD generator may, despite its intrinsic efficiency limitations, prove effective for specialized airborne applications.

In our review of the open literature, we discovered only one paper directly addressing this concept on an experimental basis, and it was published by researchers from the Krzhizanovsky Power Institute in Moscow.[6] Their motive at the time was the development of peak/emergency power stations that would operate on natural gas. Because detonation-driven MHD power avoids the need for a high-temperature heat exchanger, a large compressor station, and a complex dc-to-ac conversion system, they realized that the intrinsic energy conversion inefficiencies associated with this device could be offset by the extremely low capital costs of construction.

These researchers used a natural-gas/oxygen-fired detonation tube seeded with a K_2CO_3 aqueous solution to drive a 16-mm diam linear MHD channel subjected to a 0.23 T magnetic induction, and were able to extract electrical power while running the system at repetition rates approaching 100 cps for a duration of 2 h. The channel electrodes were segmented; however, the active MHD length was not specified. Observed cycle-to-cycle variations in detonation velocity did not exceed 1.5%, and the wall heat flux accounted for 25% of the released combustion energy. The power output peaked at $\sim 0.1 W_e$ at a load impedance near 10 mho. The maximum effective electrical conductivity measured during these tests was $\langle \sigma \rangle = 3.3$ mho/m. These test results validated the fundamental technical feasibility of pulse detonation-driven MHD power and provided us with confidence that the concept could be extended for various applications.

This paper reports recent results from an experimental study conducted at ERC facilities. The objective of these experiments was to investigate the basic engineering performance characteristics of a laboratory-scale pulse detonation-driven MHD generator. This included quantification of ionization properties behind the detonation wave and evaluation of electrical power-extraction characteristics from a short-length continuous-electrode Faraday channel. The experimental results reported here are only for stoichiometric mixtures of acetylene and oxygen using an atomized spray of cesium hydroxide dissolved in alcohol as an ionization seed in the active MHD region.

Experimental Apparatus

ERC's laboratory-scale detonation tube is closed at one end, and various plasma diagnostic and MHD channels can be attached to the open end using an area transition adapter. A custom-fabricated permanent magnet assembly was available for establishing MHD interaction in the channel. All of our experiments were conducted in a single-shot mode where the system is evacuated, charged to atmospheric pressure with premixed combustibles, and ultimately detonated using a high-voltage spark discharge near the closed end of the tube. During this process, a thin membrane separates the chamber volume from the surrounding atmosphere until it is ruptured by the detonation wave. Ionization seed is introduced using an atomizing injector that is located near the open end of the detonation tube and oriented in such a way as to direct the seed spray along the length of the attached channel. The design/configuration of the individual components making up our experimental apparatus are discussed in detail in the following subsections.

Detonation Tube

The detonation tube is constructed from a 1-m-long section of schedule-40 steel pipe having a nominal i.d. of 2.54 cm. The detailed configuration of our tube is shown in Fig. 1. The head of the detonation tube is sealed with a pipe cap in which fitting connectors

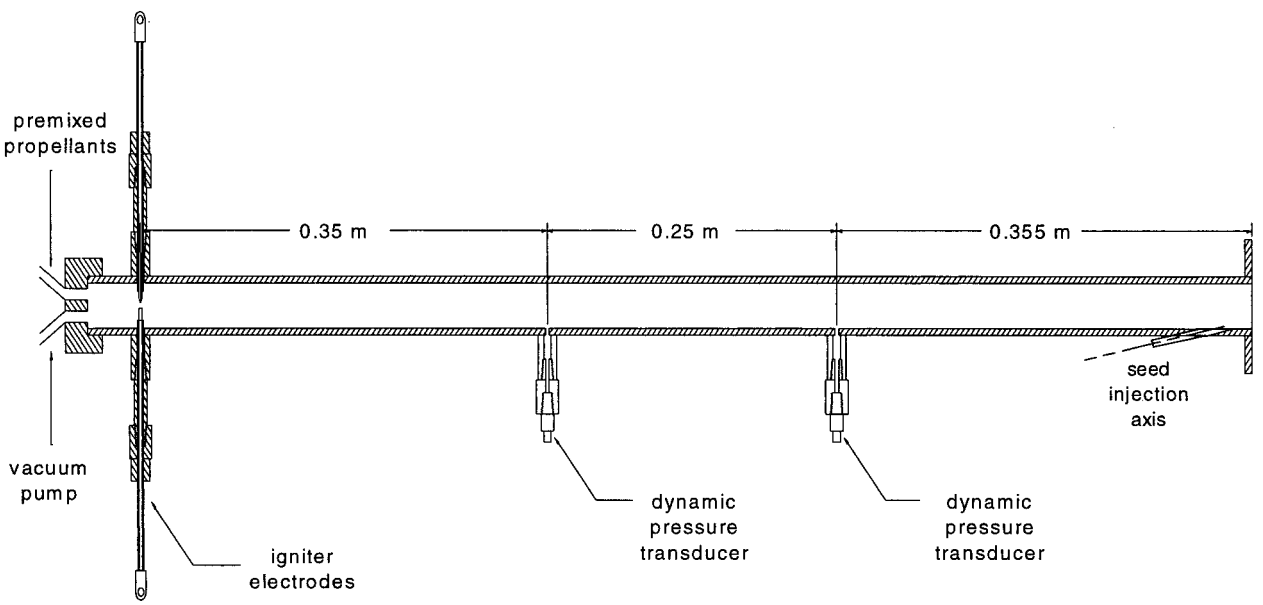

Fig. 1 Schematic of the 1-m-long laboratory-scale pulse detonation tube with 2.54-cm bore.

have been installed for evacuating the tube and for introducing premixed combustibles. The open end is flanged for attachment of an area transition adapter and diagnostic/MHD channels.

A pair of high-voltage igniter electrodes were fabricated from copper pins with tungsten tip inserts and located near the closed end of the tube. The tip of the igniter cathode was ground to a point to increase the local electric field intensity and thereby reduce the required breakdown voltage across the 3-mm gap. The discharge energy for directly initiating the combustion detonation wave is created by discharging the energy stored in an LRC circuit, which is closed using a solenoid-operated mechanical switch. The oscillating electric field that drives the gas discharge was observed to decay completely within 100 μs. The circuit discharges a 2-μF energy storage capacitor that has been precharged to 10 kV, yielding an ignition energy source of magnitude $W_{ign} = \frac{1}{2}CV^2 \sim 100$ J. This value exceeds the minimum ignition energy necessary for direct initiation of acetylene/oxygen mixtures by several orders of magnitude.[7] This level of ignition energy provides assurance that true detonation conditions are attained.

Two dynamic pressure transducers are mounted in the tube at roughly equal distances from either end, such that the separation distance between them is exactly 0.25 m. These sensors provide an indication of detonation wave strength and are used for time-of-flight measurements of detonation wave speed. For our data sampling rate of 200 kHz, we encounter an uncertainty of ± 5 μs in the time-of-flight measurement.

Atomizing Seed Injector

An electrically activated atomizing fuel injector from an automotive engine was adapted for injection of ionization seed. The injector was mounted to the detonation tube and oriented so that the spray cone was directed downstream into the channel region. For seed material, we used a 30% solution (by mass) of cesium hydroxide in a methanol carrier. In conducting each test, we first activated the pressurized injector for 50 ms and then delayed the ignition trigger by 100 ms. Based on our calibrated volumetric injection rate of 3 cm^3/s, we estimate that 0.15 cm^3 of seed solution was injected per shot. We were unable to ascertain the actual seed fraction in the channel, however, due to poorly defined atomization characteristics, attachment of the seed material to the wall, and uncertainty in the seed distribution.

Plasma Diagnostic Channel

A plasma diagnostic channel was also designed and fabricated to quantify the electrical properties of the ionized gas behind the detonation front. This short-length axisymmetric diagnostic channel, which has the same i.d. as the detonation tube, is shown in Fig. 2. The main body is machined from G-11 phenolic and is fitted with a set of 1.6-mm copper electrode segments to which a preset electric potential can be applied. These electrodes are mounted flush with the wall and maintain a contact angle of 60 deg with the flow. The channel is also equipped with two tungsten wire electrostatic probes for measuring the local plasma potential in the core. They are located 5 mm above the anode and cathode surfaces, respectively. Together, the discharge electrodes and electrostatic probes form a four-electrode electrical conductivity probe.[8] A tap for a dynamic pressure transducer is located at the same axial location. In addition, a sapphire window port was integrated into the design so that the gas discharge process and detonation wave passage could be observed optically. The diagnostic channel was fabricated for direct mating with the detonation tube.

Permanent Magnet Assembly

A permanent magnet assembly was available to support in-house testing efforts. This magnet is composed of individual segments that are 2 in. wide and contain eight $2 \times 2 \times 1$ in. low-grade rare earth magnetic blocks ($BH_{max} = 35$ MGOe) and four $2 \times 2 \times \frac{1}{2}$ in. high-grade rare earth magnetic blocks ($BH_{max} = 45$ MGOe), each. A total of six segments combine to form a 30-cm-long permanent magnet assembly that provides a uniform magnetic induction of 0.6 T over a 3.8-cm air gap.

Faraday MHD Channel

A continuous-electrode Faraday MHD channel was also designed and fabricated to fit the available permanent magnet assembly. This constant-area channel, shown in Fig. 3, has an active MHD length of 30 cm. The internal flow passage is rectangular in shape with a 2.54-cm height between electrodes and a 2.0-cm width between sidewalls. The main body of the channel is fabricated from G-11 phenolic, as is the area transition adapter connecting the tube to the channel. The copper-alloy electrodes include pressure taps at four locations along the active channel length.

Experiment Control/Signal Acquisition

A personal computer with appropriate I/O hardware was used to sequence and control the experiments and to acquire four channels of high-speed data at a sampling rate of 200 kHz per channel. A 50-MHz two-channel digital oscilloscope was also utilized to capture fast signal transients. High-speed diagnostic measurements available for physical interpretation include the following:

1) Static pressure fluctuations at the wall to define the speed and strength of the combustion detonation wave.

2) Radiative emission through the window port of the diagnostic channel for additional definition of detonation wave morphology and structure.

3) Electrostatic probe voltages for measuring local plasma potential relative to the cathode.

4) Anode-to-cathode voltages and currents in the plasma diagnostic channel circuit as a means of deducing the electrical properties of the ionized gas.

5) Load voltages and currents in the MHD channel circuit as a means of deducing power extraction characteristic.

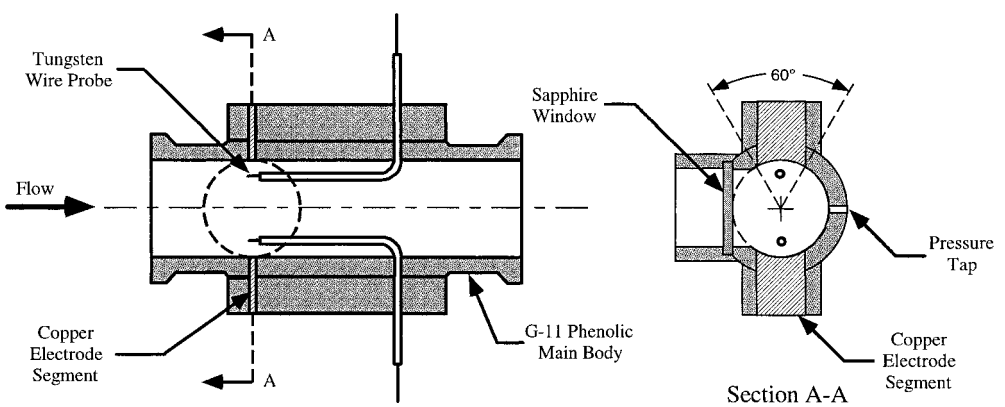

Fig. 2 Schematic of windowed axisymmetric plasma diagnostic channel. Note that the wall-mounted discharge electrodes can be combined with the electrostatic probes in the core to form a four-electrode electrical conductivity probe.

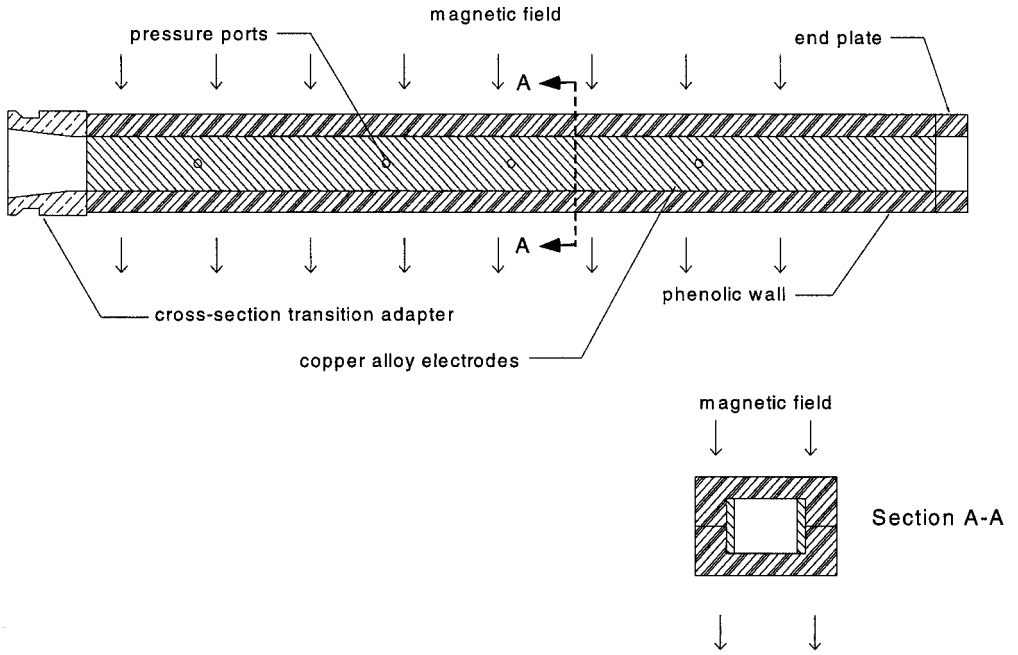

Fig. 3 Schematic of the 0.3-m-long continuous-electrode Faraday MHD channel. Active region is 2.54 cm in height and 2.0 cm in width.

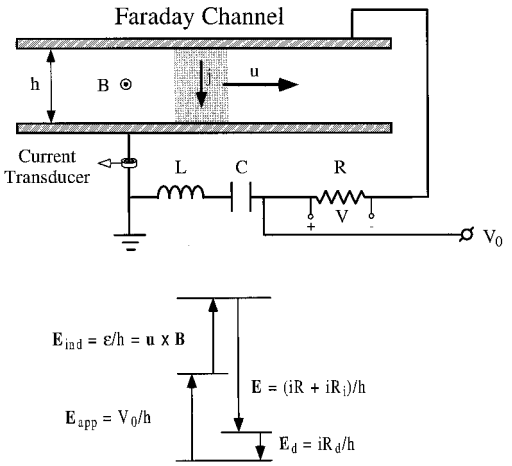

Fig. 4 LRC active loading circuit and electric potential level diagram for idealized electrodynamic model.

Electrodynamic Model

A simple first-order electrodynamic model was developed as an aid to the interpretation of experimental results and as a basis for developing generalized scaling laws. In this model we consider a uniform slug of burned ionized gas moving with velocity $\boldsymbol{u}$ through a channel of height h that is subjected to an applied magnetic induction $\boldsymbol{B}$, and which has wall electrodes for directly coupling MHD interaction in the flowing plasma with an LRC active loading circuit. In general, the slug thickness δ may be less than the active channel length L. We assume a uniformly distributed current density $\boldsymbol{j}$ in the plasma slug, and we neglect Hall effects due to the very high-pressure levels experienced behind the combustion detonation wave. Furthermore, we assume that the magnetic Reynolds number is much less than 1, and neglect flux compression effects. The electrodynamic model and potential level diagram are shown in Fig. 4. The active loading circuit includes the possibility of precharging the capacitor to an applied voltage v_0 as a means of simulating a higher effective magnetic induction, $\boldsymbol{B}_{\text{eff}}$.

The effective induced electric field $\boldsymbol{E}_{\text{eff}}$ in the channel is the sum of the induced Faraday field associated with the applied magnetic induction $E_{\text{ind}} = |\boldsymbol{u} \times \boldsymbol{B}| = \varepsilon / h$, and the applied field $E_{\text{app}} = v_0 / h$. Thus, the effective induced potential in the channel may be written as

$$\varepsilon_{\text{eff}} = \varepsilon + v_0 = uBh + v_0 = uB_{\text{eff}}h \tag{1}$$

where

$$B_{\text{eff}} = B + (v_0/uh) \tag{2}$$

Requiring that the current have a positive magnitude in the direction of $\boldsymbol{u} \times \boldsymbol{B}$, Kirchoff's voltage law implies that the effective induced emf $\varepsilon_{\text{eff}} = uB_{\text{eff}}h$ be balanced by voltage drops resulting from the external load R, internal resistance of the plasma R_i, and a lump potential loss $v_d = iR_d$:

$$\varepsilon_{\text{eff}} = uB_{\text{eff}}h = iR + iR_i + iR_d = V + jh/\sigma + v_d \tag{3}$$

where we have introduced the current density $j = i/A$, and the electrical conductivity $\sigma = h/(AR_i)$. The lump-loss term v_d is introduced to account for plasma nonuniformities, near-electrode potential drops, emission losses, current concentrations, as well as possible current leakage and shortings.[9] We are assuming that $v_0 \approx$ const during passage of the plasma slug, and because the inductance in our loading circuit is extremely low, we have neglected inductive energy storage terms. Thus, Eq. (3) may be further manipulated to obtain

$$uB_{\text{eff}} = V/h + j/\sigma + v_d/h = E + j/\sigma + E_d \tag{4}$$

where i is the load current and V is the terminal voltage measured across the load. Solving Eq. (4) for j yields the generalized Ohm's law for the generator:

$$j = \sigma(uB_{\text{eff}} - E - E_d) \tag{5}$$

Following a modeling strategy analogous to Wu,[9] we define a dimensionless voltage drop Δ as

$$\Delta = \frac{v_d}{uB_{\text{eff}}h} \tag{6}$$

This engineering parameter represents a direct measurement of the voltage drop losses relative to the effective emf of the generator.

For an MHD generator, the load factor K is defined as

$$K = \frac{\text{electric power delivered to load}}{\text{useful electric power generated}} = \frac{i^2R}{i^2R + i^2R_i} \tag{7}$$

and elimination of v_d for Δ yields the relation

$$K = \frac{iR}{iR + iR_i} = \frac{V}{uB_{\text{eff}}h - v_d} = \frac{E}{uB_{\text{eff}}(1-\Delta)} \tag{8}$$

By substituting Eqs. (6) and (8) into the generalized Ohm's law, we obtain an expression for the current density in the generator:

$$j = \sigma u B_{\text{eff}}(1-\Delta)(1-K) \tag{9}$$

In addition, an expression for the generator power density follows from the basic definition $\mathcal{P} = \boldsymbol{j}\cdot\boldsymbol{E}$, and from the use of Eqs. (8) and (9) to eliminate E and j:

$$\mathcal{P} = \boldsymbol{j}\cdot\boldsymbol{E} = \sigma u^2 B_{\text{eff}}^2(1-\Delta)^2 K(1-K) \tag{10}$$

The maximum power density occurs when $d\mathcal{P}/dK = 0$, such that $K = \frac{1}{2}$ for optimum performance. It should be clear from Eq. (10) that when the induced emf is limited due to small channel height and/or low magnetic induction, the lump potential loss v_d can have a profound affect on generator performance.

The Lorentz body force acting on the plasma slug may be defined in terms of the charged particle drift velocity $\boldsymbol{w}$:

$$\boldsymbol{f} = nq(\boldsymbol{w}\times\boldsymbol{B}) = \boldsymbol{j}\times\boldsymbol{B} \tag{11}$$

and substitution of Eq. (9) into Eq. (11) yields the actual Lorentz body force experienced by the plasma slug:

$$f = |\boldsymbol{j}\times\boldsymbol{B}| = \sigma u B_{\text{eff}} B(1-\Delta)(1-K) < |\boldsymbol{j}\times\boldsymbol{B}_{\text{eff}}| \tag{12}$$

Thus, for the active loading circuit, $f \propto B_{\text{eff}}B$, assuming that all other factors remain constant. However, for true similarity, the Lorentz body force should vary in proportion to B_{eff}^2, not BB_{eff}, and the MHD interaction level is too small by the factor $B_{\text{eff}}/B = 1 + v_0/(uBh)$.

More directly stated, the magnetic interaction parameter S (work done by Lorentz force/inertial energy of flowfield), based on the use of an effective magnetic induction, is less than that required for proper simulation of the push work. That is

$$S = R_m R_h = \frac{\sigma_0 L_0 B_{\text{eff}} B_0}{\rho_0 u_0} < \frac{\sigma_0 L_0 B_{\text{eff}}^2}{\rho_0 u_0} = S_{\text{required}} \tag{13}$$

where R_m (Lorentz force/magnetic body force) is the magnetic Reynolds number, R_h (magnetic body force/inertial force) is the magnetic force number, and the subscript 0 refers to reference conditions. The actual rate at which the ionized gas does push work in the actively loaded channel is

$$\mathcal{P}_p \approx fu = \sigma u^2 B_{\text{eff}} B(1-\Delta)(1-K) \tag{14}$$

When $C = 0$ and there is no applied voltage, $B_{\text{eff}} = B$ and the passive load model is recovered.

Experimental Results

Detonation Characteristics

As a prelude to operating the detonation tube, we carried out detonation calculations using the NASA SP-273 chemical equilibrium code.[10] The stoichiometric mixture ratio was based on the combustion products being either CO_2 or H_2O, and the initial static pressure and temperature in the unburned gas was $p_1 = 1$ atm and $T_1 = 300$ K, respectively. Assuming Chapman–Jouguet (C–J) detonation wave structure, this program computes, among other parameters, the pressure/temperature ratio across the detonation front, the detonation wave velocity D relative to the duct, and the speed of sound of the burned gas a_2 relative to the detonation wave. For C–J conditions, the burned gas velocity is sonic relative to the detonation wave, i.e., $M_2 = 1$, and $u_2 = a_2 = \sqrt{(\gamma_2 R_2 T_2)}$. We are then able to deduce the burned gas velocity relative to the tube using the relation $u_b = D - u_2 = D - a_2$, where u_b corresponds to the slug velocity in our electrodynamic model. The major results, summarized next, provide a baseline performance benchmark for our experiments: $D = 2425$ m/s, $a_2 = 1317$ m/s, $u_b = 1100$ m/s, $p_2/p_1 = 33.64$, and $T_2/T_1 = 14.04$.

The computed detonation wave speed is in good agreement with widely accepted experimental measurements,[11] and we expect a static pressure $p_2 = 33.64$ atm (495 psia) and a static temperature $T_2 = 4200$ K behind the detonation wave based on initial conditions in the tube.

Experiments were then conducted in our apparatus to confirm the attainment of true detonation conditions. As an example, representative pressure waveforms acquired from the dynamic pressure transducers during a typical shot are presented in Fig. 5. We attribute the slightly elevated pressure levels near the ignition source to overdriven detonation as being caused by our use of an extremely high-ignition energy (~100 J). Once the detonation wave has traversed two-thirds the length of the tube, however, C–J conditions are fully attained, and the pressure rise across the detonation front is found to be in close agreement with the baseline theoretical prediction. As further evidence, we note that cross correlation of these

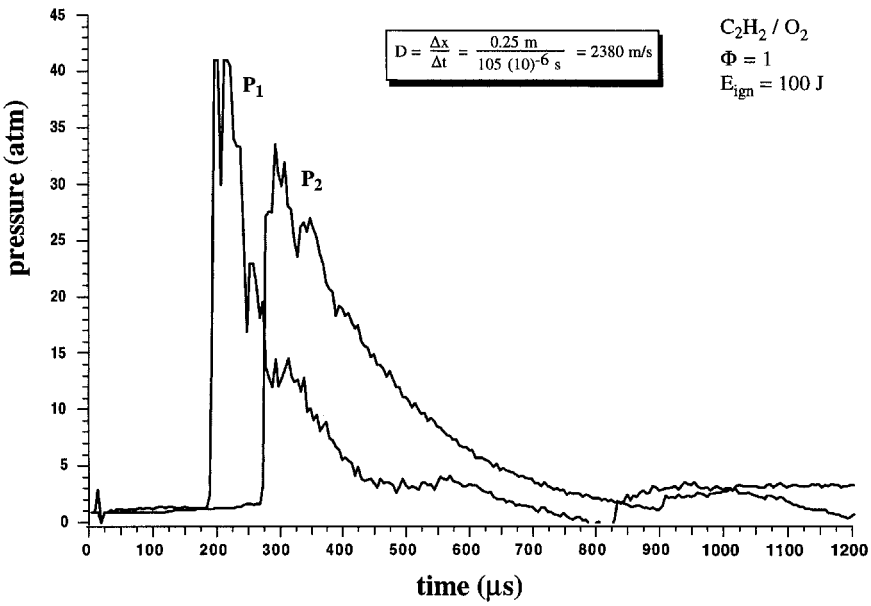

Fig. 5 Representative pressure waveforms as measured in the detonation tube during a typical shot.

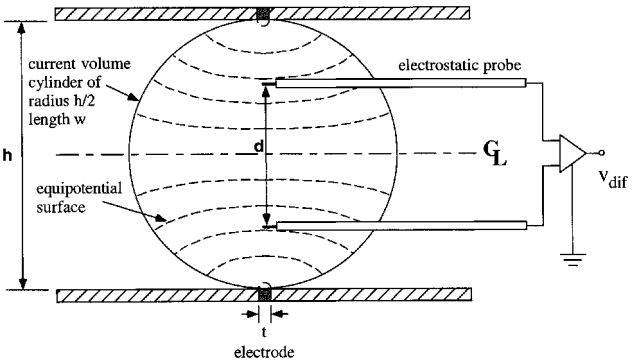

Fig. 6 Illustration of the assumed current distribution between discharge electrodes in the plasma diagnostic channel.

waveforms yields a time delay of 105 μs and a detonation wave speed relative to the tube of 2380 m/s. This quantity is also in good agreement with the baseline calculations. Repeated experiments showed little variation in the preceding results, giving us confidence that true detonation conditions were being reliably achieved.

Plasma Diagnostics

With the plasma diagnostic channel attached to the end of the detonation tube, further experiments were conducted to quantify the ionization properties of the burned gas following the detonation front. Of utmost interest were 1) the level of electrical conductivity achieved, 2) the magnitude of near-electrode potential losses, and 3) the definition of structural features.

In these experiments, an electric breakdown potential of 100 V was applied between the wall electrodes during passage of the detonation wave. The resulting discharge of current through the ionized gas allowed us to deduce bulk electrical properties from the measured electrostatic probe voltage waveforms and the anode-to-cathode current waveform. Although highly intrusive, this technique provides an effective measurement of major electrical parameters of engineering interest.

The single most important parameter indicating ionization quality is the electrical conductivity. In this work, we utilize two intrusive probing methods for determining an effective bulk value based on Ohm's law, $j = \sigma E$. They are classified as two- and four-electrode probes, respectively.[8] Application of these probing methods can lead to dubious results, however, due to uncertainty in the current distribution within the ionized gas. This uncertainty in current distribution makes the accurate assessment of current density and derived quantities such as electrical conductivity problematic.

Reliable deduction of these electrical parameters requires careful consideration of electrode geometry and probe configuration. When using point electrodes, e.g., fundamental theoretical considerations and a vast array of empirical evidence has demonstrated that the current tends to uniformly diffuse into a spherical distribution having a diameter equal to the anode-to-cathode gap in the ionized gas.[§] For the thin electrode segments in our diagnostic channel, we therefore assume, based on symmetry arguments, that the current will uniformly diffuse into a circular cylinder having a diameter equal to the channel height h and a depth equal to the electrode width w. This geometry is illustrated in Fig. 6.

The electric field between the electrodes can be modeled using two-dimensional line sources, where the electric potential ϕ at any point (x, y) from the centerline of the electrodes and the centerline of the channel is obtained by summing the contribution due to each line source:

$$\phi = \Lambda \ln\sqrt{x^2 + (h/2 - y)^2} - \Lambda \ln\sqrt{x^2 + (h/2 + y)^2} \qquad (15)$$

The constant Λ represents the source strength and can be evaluated by imposing the known voltages on the top and bottom electrodes. The electric field vector $\boldsymbol{E}$ can be determined from the relation $\boldsymbol{E} = -\text{grad}\,\phi$. The equipotential surfaces within the assumed cylindrical current volume are illustrated schematically in Fig. 6.

Two-Electrode Probe

In the two-electrode method, we first consider a cross section of the assumed cylindrical current volume and define the current density j through an equipotential surface A_{es} as

$$j = i/A_{es}\xi \qquad (16)$$

where i is the measured total current, and ξ has been introduced as an efficiency coefficient of order unity. As a simplification to the analysis, we approximate the area of the equipotential surfaces as the product of the cylinder chord c and the electrode width w:

$$A_{es} \approx wc = w2\sqrt{h\zeta - \zeta^2} \qquad (17)$$

where ζ is the radial distance from the electrode surface to the chord, and $A_{es} = wh$ when $\zeta = h/2$. Upon substituting Ohm's law, we obtain an expression for the local electric field in the form

$$E = \left(\frac{i}{w\xi\sigma 2}\right)\left(\frac{1}{\sqrt{h\xi - \xi^2}}\right) \qquad (18)$$

Then, we may integrate for the applied voltage across the channel using Eq. (18):

$$v_{app} = 2\int_0^{h/2} E\,\mathrm{d}\zeta = \frac{i}{w\xi\sigma}\int_0^{h/2} \frac{\mathrm{d}\zeta}{\sqrt{h\xi - \xi^2}} \qquad (19)$$

Evaluation of this integral yields the final desired expression for electrical conductivity in terms of the primary measurement parameters:

$$\sigma = \left(\frac{\pi}{2}\right)\left(\frac{i}{v_{app}w\xi}\right) \qquad (20)$$

Four-Electrode Probe

Unfortunately, the two-electrode probe tends to suffer from near-electrode potential drops and nonohmic contact resistances, and a four-electrode probe is usually recommended. In the four-electrode probe, a pair of electrostatic probes are introduced between the anode and cathode to measure the voltage drop v_{dif} over a distance d in the core of the flow. With this configuration, the parasitic resistance problems are minimized.

The critical assumption is the definition of the cross-sectional area for computing current density in the core. Here, we take the cross section of the current volume cylinder at the centerline as the effective area such that $A_{eff} = wh$. Thus, the effective current density in the core j_{eff} takes the form:

$$j_{eff} = i/A_{eff}\xi = i/wh\xi \qquad (21)$$

The expression for electrical conductivity using the four-electrode configuration follows from a direct application of Ohm's law:

$$\sigma = j_{eff}/E = (i/wh\xi)(d/v_{dif}) \qquad (22)$$

Ionization Quality/Structure

A seven-waveform ensemble average of the effective current density in the diagnostic channel, as computed from Eq. (21), is shown in Fig. 7. In this work we take ξ to be unity. These measurements demonstrate the emergence of primary and secondary wave structures. The primary wave is associated with the passage of the burned gas behind the detonation front, but the physical mechanism responsible for the trailing secondary wave is not clear. The emergence of a conductive secondary wave structure has been observed in previous detonation experiments with oxy-acetylene mixtures.[6,12–14] Generally speaking, these experiments indicate a secondary wave structure that may be associated with delayed chemical reactions behind the detonation front. As such, the induction period never exceeded more than a few hundred microseconds. In Fig. 7, however, the time delay between the primary and secondary waves is rather long

[§]Bityurin, V. A., private communication, Inst. of High Temperatures (IVTAN), Moscow, 1998.

(~1.5 ms), and the appearance of the secondary waveform shows a temporal correlation with the extreme tail of the measured pressure waveform. Therefore, the secondary waveform we observe here is more likely associated with flow reversal in the channel. The peak current density in the primary and secondary waves was roughly 2 and 0.5 A/cm^2, respectively.

Normalized seven-waveform ensemble averages of static pressure and radiative emission in the diagnostic channel are shown in Fig. 8. In this case, the hump riding on the trailing edge of the pressure waveform is indicative of a secondary compression wave similar to that observed by Cher and Kistiakowsky.[13] Radiative emission integrated over the optical region is very constant during passage of the primary conductive wave, seemingly suggestive of fairly uniform thermal conditions; however, the measured electrical conductivity, presented next, does not corroborate this interpretation.

A seven-waveform ensemble average of the differential electrostatic probe voltage v_{dif} is shown in Fig. 9. Only data corresponding to passage of the primary wave were captured. Note that the voltage drop between probes was roughly 40 V during this event. By assuming $v_d \approx v_{app} - v_{dif}$, we were also able to estimate the dimensionless voltage drop in the channel using Eq. (6), where $B_{eff} = v_{app}/uh$. This estimation yielded $\Delta \approx 0.6$.

Ensemble-averaged electrical-conductivity waveforms are shown in Fig. 10 based on two- and four-electrode probing techniques. Agreement between the two methods is very good. The peak electrical conductivity in the primary wave is seen to be approximately 6 mho/m. For comparative purposes, we carried out calculations for the electrical conductivity and electron number density in the burned gas as a function of the seed mole fraction. We used a modified version of the NASA SP-273 chemical equilibrium code in which the

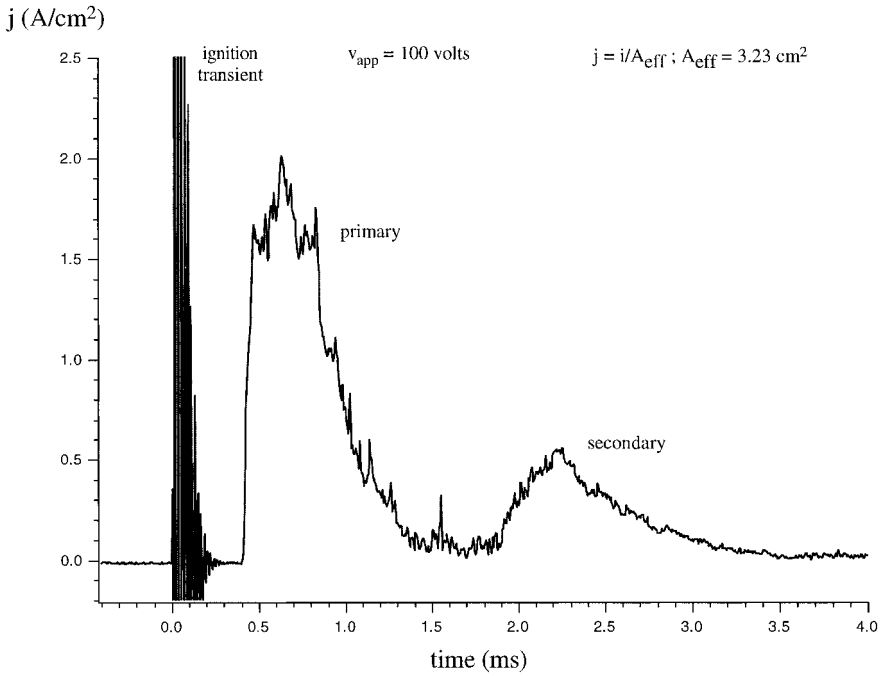

Fig. 7 Seven-waveform ensemble average of the effective current density in the plasma diagnostic channel. Note the delayed appearance of a secondary wave structure.

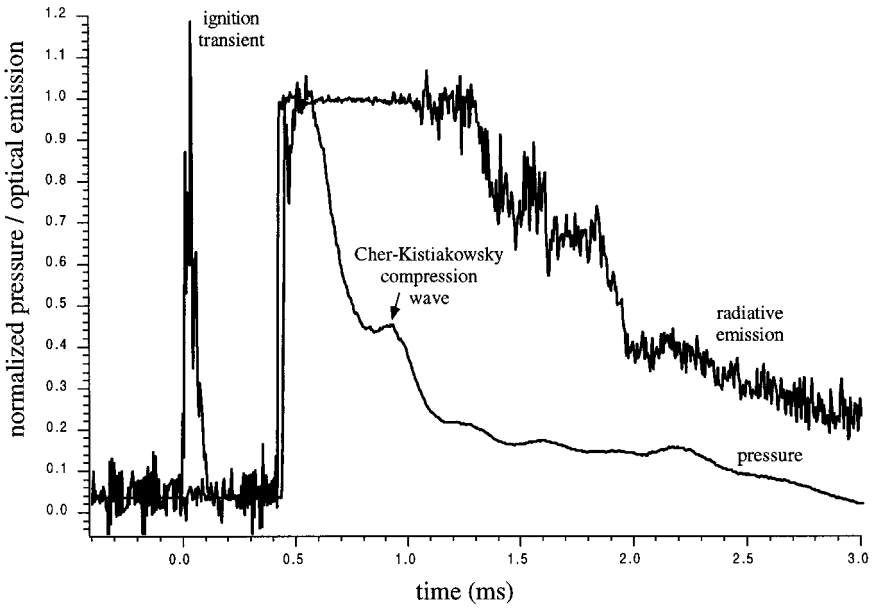

Fig. 8 Seven-waveform ensemble average of static pressure and radiative emission in the plasma diagnostic channel. Waveforms have been normalized using peak values in the detonation front. Note the emergence of a receding Cher–Kistiakowsky secondary compression wave.[13]

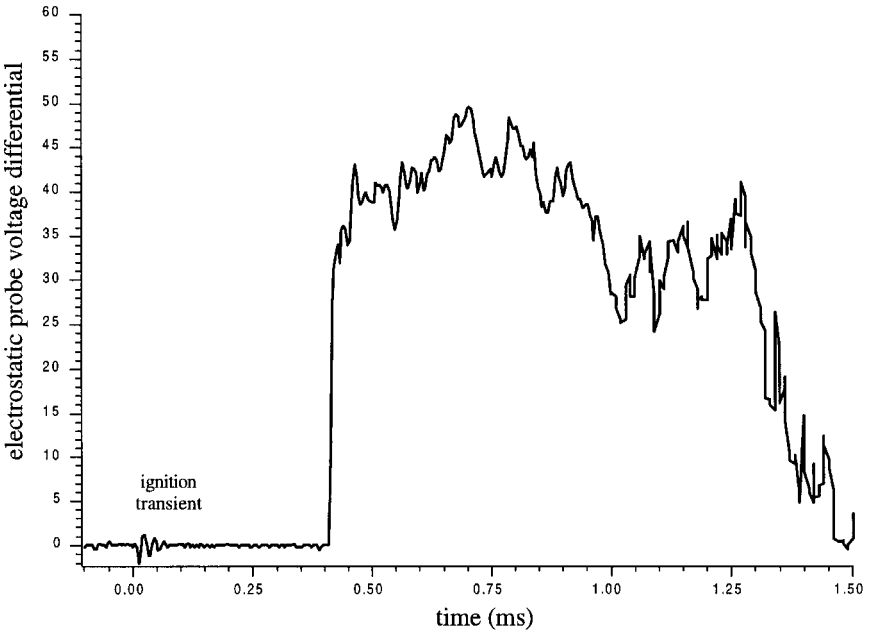

Fig. 9 Seven-waveform ensemble average of the electrostatic probe voltage differential in the plasma diagnostic channel.

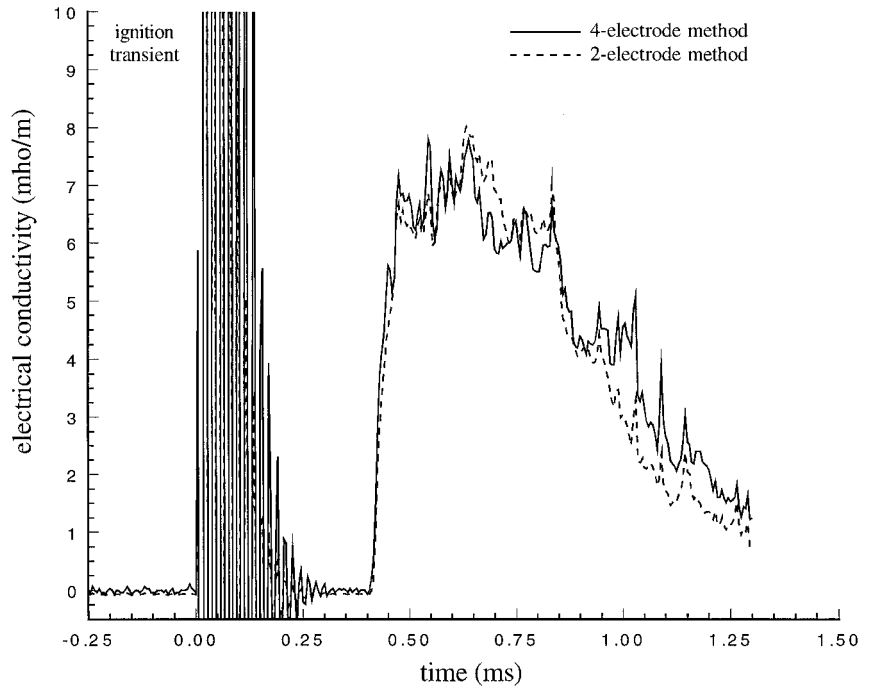

Fig. 10 Seven-waveform ensemble average of electrical conductivity in the plasma diagnostic channel based on both four- and two-electrode probing techniques.

plasma electrical transport properties are computed according to Frost.[15] These results are shown in Fig. 11.

MHD Power Extraction

MHD power-extraction experiments were conducted with the short-length continuous-electrode Faraday channel attached to the detonation tube and placed in the bore of the permanent magnet assembly. In these experiments, the channel was connected to the active loading circuit shown in Fig. 4 to simulate higher effective magnetic induction. Our principal objectives were as follows: 1) to demonstrate pulse detonation-driven MHD energy conversion, 2) to map the load line characteristics of the generator, and 3) to estimate energy density characteristics for engineering scaling purposes.

Open-Circuit Voltage/Burned Gas Velocity

Our first task was to acquire the open-circuit characteristics of the generator by applying a very high-load impedance with the capacitor removed from the circuit. Figure 12 shows a typical terminal voltage waveform under these conditions, where the waveform represents a direct measurement of the peak Faraday potential in the generator, $V_{oc} = uBh \approx 10$ V. Obviously, the small scale of our device greatly inhibits performance in that the near-electrode potential drop is of the same order as the Faraday potential. Dividing this waveform by

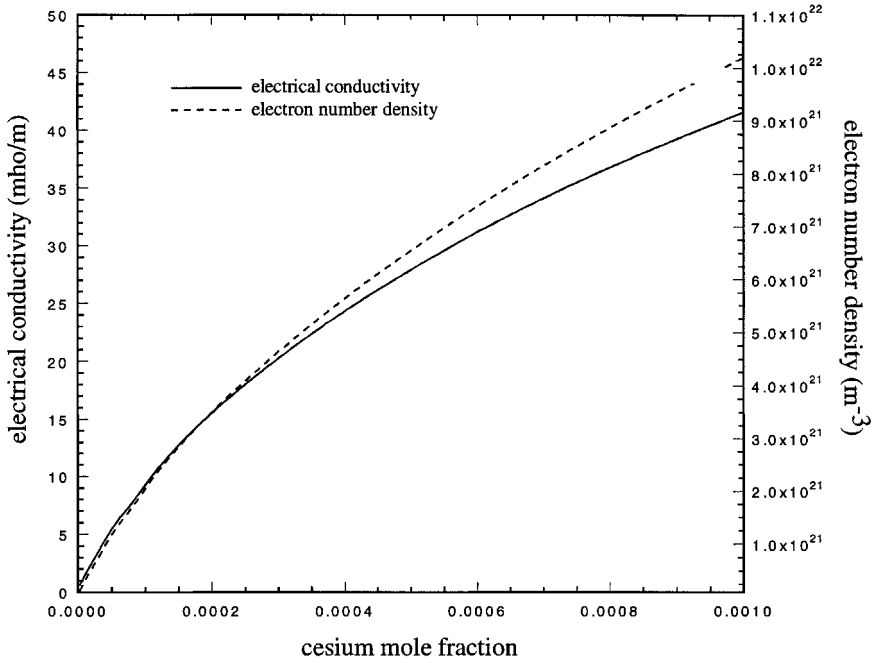

Fig. 11 Computed electrical conductivity and electron number density behind the detonation front based on a modified version of the NASA SP-273 chemical equilibrium code where plasma electrical transport properties are computed according to Frost.[13]

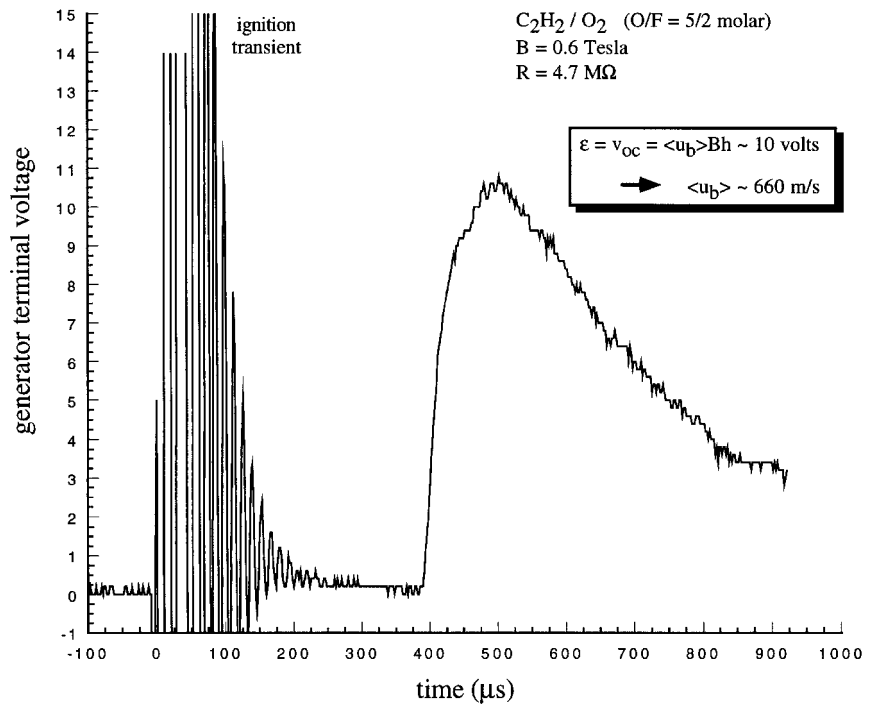

Fig. 12 Generator terminal voltage waveform under open-circuit loading conditions. Division of this waveform by *Bh* yields an effective burned-gas velocity waveform in the channel.

the known magnetic induction (0.6 T) and the channel height (0.0254 m), we deduce an effective burned gas velocity relative to the tube of $\langle u_b \rangle \sim 660$ m/s. This value can be compared with the theoretical equilibrium prediction specified earlier in the text (1100 m/s). The effective burned gas velocity is lower because the velocity behind the detonation wave must decay to zero at the closed end of the tube.

Load-Line Characteristics

We mapped out the load-line characteristics of the generator for five values of the applied forward voltage v_0: 0, 25, 50, 75, and 100 V. For each applied forward voltage, we measured current waveforms for the following set of load impedance values: 0, 0.0175, 0.098, 1, 5, 10, and 100 Ω. Representative results are shown in Fig. 13 for $v_0 = 50$ V. As expected, the peak current attains its maximum value under short-circuit conditions and falls with increasing load impedance. We also note the emergence of a delayed relatively weak secondary pulse that is associated with the flow reversal effect identified in Fig. 7.

Generator load lines were constructed based on measured peak values for current and load voltage. The results, normalized with respect to the short-circuit current and the open-circuit voltage, are shown in Fig. 14. The characteristic shape exhibits linear features away from the extreme loading conditions. At extreme loading

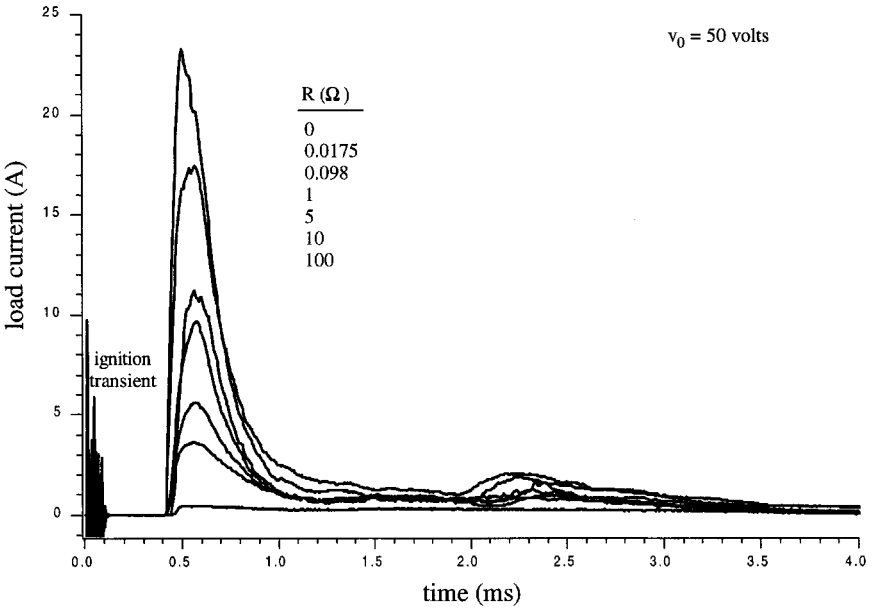

Fig. 13 Measured current waveforms for various load impedances with v_0 = 50 V. Peak current scales inversely with load impedance.

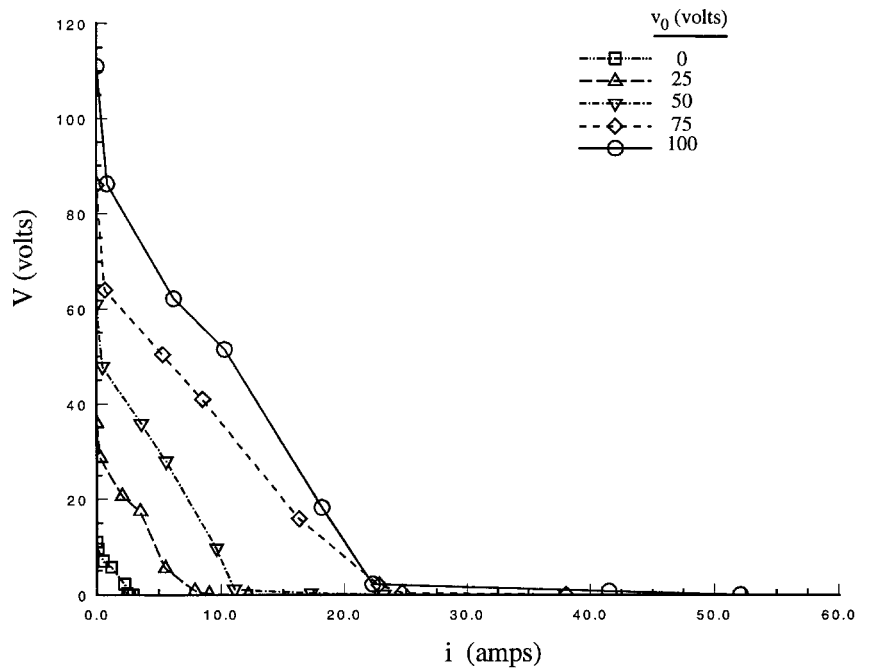

Fig. 14 Measured load-line characteristics of the pulse detonation MHD generator.

conditions, there are very strong nonlinear effects. This behavior is not understood at this point in time.

Energy Density Scaling Parameter

From an engineering point of view, it is advantageous and useful to express the power-extraction characteristics of the generator in terms of a performance-related scaling parameter. Once we develop quantitative estimates for this parameter, we can then project device performance at practical scales. Although it is difficult to extrapolate the performance of MHD devices from laboratory scales where boundary-layer losses dominate, to a scale suitable for practical application where core flow processes dominate, we adopt this approach as a conservative estimate of scaling effects. Under virtually all circumstances, this approach will tend to underpredict performance and will usually represent a worst-case scenario. The prediction can therefore be treated as an effective lower bound on anticipated performance.

Because electrical power output is the performance parameter of primary interest in MHD generators, we begin our development with the following definition:

$$\frac{\mathrm{d}W}{\mathrm{d}t} = u\frac{\mathrm{d}W}{\mathrm{d}x} = \mathcal{P}wh\delta \tag{23}$$

where W represents electrical work in Joules, and the power density $\mathcal{P}$ was obtained in Eq. (10). The electrical work per unit channel length per detonation pulse can therefore be written as

$$\frac{\mathrm{d}W}{\mathrm{d}x} = \frac{\mathcal{P}wh\delta}{u} \approx \frac{W_D}{L} \tag{24}$$

Here, L is the active length of the MHD channel, and W_D represents the electrical energy transferred per detonation pulse. We further

note that W_D can be empirically evaluated by integrating over the measured output waveform of the generator

$$W_D = \int i^2 R \, dt + \mathcal{L} \int i \frac{di}{dt} dt \approx \int i^2 R \, dt \tag{25}$$

where the inductance $\mathcal{L}$ is very small in our circuit and can be neglected.

Equation (24) can now be manipulated to obtain the desired energy density scaling parameter in the form:

$$W_D/whL = \mathcal{P}\delta/u \tag{26}$$

This parameter has units of J/m^3 and represents the electrical energy produced per unit channel length per unit channel height per unit channel width per detonation. By eliminating $\mathcal{P}$ using Eq. (10), we obtain the final working relation

$$(W_D/whL)(1-\Delta)^{-2} = \delta\sigma u B^2 K(1-K) \tag{27}$$

We note that the parameters on the right-hand side (RHS) of Eq. (27) are assumed to be independent of device scale. Thus, once the energy density W_D/whL is empirically evaluated and one is able to make appropriate assumptions concerning the scaling of Δ, it becomes possible to extrapolate performance at increased scales.

A comparison of measured and theoretical predictions for the energy density scaling parameter is presented in Fig. 15 as a function of load impedance. The empirical value was obtained by integrating Eq. (25) using measured current waveforms and dividing by the known active channel volume. The theoretical predictions were computed from Eq. (27) using the following device parameters: $\Delta = 0.6$, $\delta = 0.3$, $\sigma = 6$ mho/m, $u = 1100$ m/s, $B = B_{\text{eff}} = 0.6 + v_0/uh$ T, and $h = 0.0254$ m. Agreement is reasonably good given the uncertainty in parameter values. The measured peak electrical energy density ranged from 10 to 10^3 J/m^3 when the effective magnetic induction was varied from 0.6 to 4.2 T. Clearly, the performance of this MHD device is limited by scale and near-electrode potential losses.

The results also show peak power extraction shifting from a load impedance of 10 Ω when $v_0 = 0$ V, to 5 Ω when $v_0 = 100$ V. We associate this shift with decreasing internal plasma resistance as the effective magnetic induction and Joule dissipation increase. That is, optimum electrical power extraction always occurs when the load impedance and the internal impedance of the generator are matched.

We recall, at this point, that the magnetic interaction parameter S based on an effective magnetic induction is less than that required for accurate simulation of the MHD interaction level. That is, the push work done by the working medium in our experiments is much lower than would be required if the magnetic induction was equivalent to the applied field. To justify the extrapolation of our results to the practical case where $B = B_{\text{eff}}$, we are therefore forced to assume that the enthalpy extraction achievable in the nonsimulated case will be high enough to provide the required push work. We are also forced to assume weak coupling between MHD interaction level and burned gas velocity.

Extrapolation of Performance to Practical Scales

The performance of small MHD devices tends to suffer from severe boundary-layer losses, as evidenced by our experimental results, and it is advantageous to use the largest feasible scale for the desired application. Along these lines, the energy density scaling relationship defined by Eq. (25) makes it possible to extrapolate device performance to practical scales from the baseline laboratory-scale experimental results. As an example, we consider a pulse detonation MHD generator that is similar in all respects to the laboratory device with the exception of channel size and applied magnetic field. Choosing values consistent with practical implementation of this concept, we selected a channel height and width of 20 cm, an active interaction length of 1 m, and an applied magnetic induction of 2.4 T.

As a preliminary task to quantifying performance scaling with size, it is first necessary to estimate the magnitude of near-electrode potential losses in a practical device. Past experience with MHD devices, e.g., indicates that the near-electrode voltage drop can be reduced considerably below that encountered in our device, which was operated only in single-shot mode, and therefore suffered from severe cold wall effects. In principle, Δ can be reduced immensely by allowing the electrodes to operate at high-temperature extremes. Based on past experience, we anticipate being able to limit the voltage drop to no more than 10% of the induced field. Holding the RHS

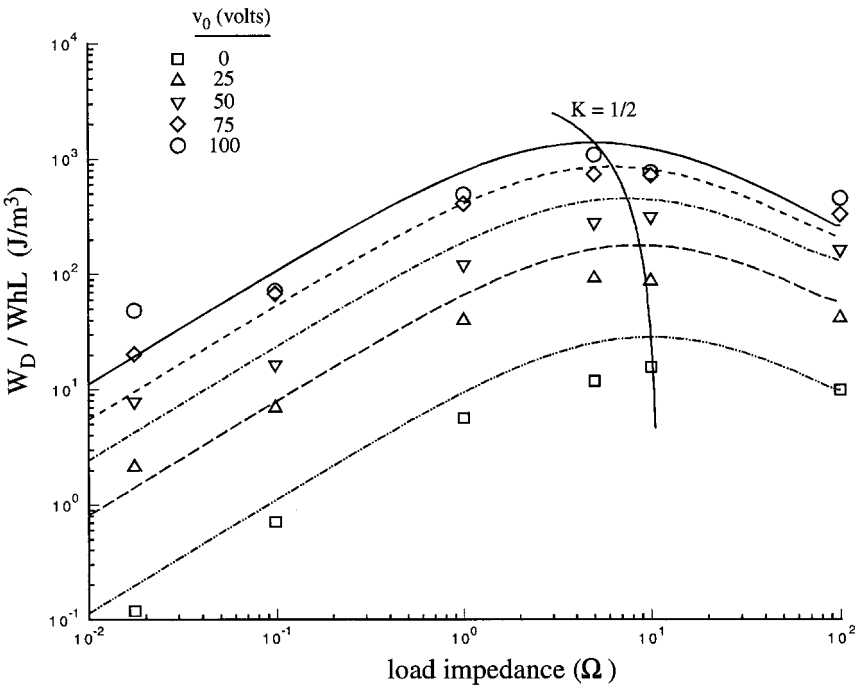

Fig. 15 Comparison of measured and theoretical predictions for the energy density scaling parameter as a function of load impedance. The theoretical predictions are shown as curves. Device parameters used in the calculations were as follows: $\Delta = 0.6$, $\delta = 0.3$, $\sigma = 6$ mho/m, $u = 1100$ m/s, $B = B_{\text{eff}} = 0.6 + v_0/uh$ T, $h = 0.0254$ m. Optimum power extraction occurs when $K = \frac{1}{2}$.

of Eq. (27) constant, we therefore estimate an energy density gain above our baseline experimental results as follows:

$$\frac{(W_D/whL)_{\Delta=0.1}}{(W_D/whL)_{\Delta=0.6}} = \frac{(1-0.1)^2}{(1-0.6)^2} = 5.1 \qquad (28)$$

For $v_0 = 50$ V, i.e., $B_{\text{eff}} = 2.4$ T, Fig. 15 yields $(W_D/whL)_{\Delta=0.6} \approx 300$ J/m^3 at optimal loading conditions. Correcting for the anticipated reduction in Δ using Eq. (26), we therefore obtain $(W_D/whL)_{\Delta=0.1} = (5.1)(300) = 1500$ J/m^3 per detonation.

The performance gain associated with increased size follows from the multiplication of the corrected energy density with the active channel volume. That is, $(W_D)_{\Delta=0.1} = (whL)\ (W_D/whL)_{\Delta=0.1} = (0.2)(0.2)(1.0)(1500) = 60$ J per detonation. Assuming a practical repetition rate $f = 100$ cps, we deduce a continuous power output of magnitude $P = f(W_D)_{\Delta=0.1} = (100)\ (60) = 6000 W_e$.

Owing to the poor seeding characteristics of our device, the preceding value represents a very conservative estimate of electrical power-generation potential. For instance, the theoretical calculations shown in Fig. 11 indicate that electrical conductivity behind the detonation front can be increased as much as five times above the level measured in our device. This would imply a direct five-fold increase in electrical power-generation performance. Optimization of seeding characteristics will require careful tailoring of injector configurations and atomization processes so that a uniform seed distribution is obtained along the channel length.

Conclusions

An exploratory series of laboratory-scale experiments have been completed with the aim of demonstrating pulse detonation MHD power extraction. In these experiments, a single-shot laboratory-scale detonation tube operating on stoichiometric oxy-acetylene mixtures seeded with an atomizing spray of cesium hydroxide in a methanol carrier was successfully used for the production of electrically conductive ionized gas behind the detonation front.

Measurements using a short-length plasma diagnostic channel attached to the end of the detonation tube confirmed the attainment of detonation conditions ($p_2/p_1 \sim 34$ and $D \sim 2400$ m/s), and yielded the following conclusions with respect to ionization quality and gasdynamic structure:

1) The measured current density in the burned ionized gas was $j \sim 2$ A/cm^2 when using an applied voltage of 100 V across the 2.54-cm height diagnostic channel.

2) The measured effective electrical conductivity of the burned ionized gas was $\sigma \sim 6$ mho/m according to both two- and four-electrode probing techniques.

3) The delayed appearance (~ 1.5 ms behind the detonation front) of a secondary conductive wave was observed that was most likely associated with flow reversal in the channel during the latter portion of the blowdown process.

4) A receding Cher–Kistiakowsky secondary compression wave[13] emerged in the acquired static pressure waveforms at a time delay of $\sim 400\ \mu$s behind the detonation front.

5) The measured dimensionless near-electrode voltage drop was $\Delta \sim 0.6$.

Power-extraction experiments were conducted using a short-length continuous-electrode Faraday channel. The channel was placed in the bore of a 0.6-T permanent magnet assembly and attached to an active loading circuit to simulate higher effective magnetic induction. The following conclusions were reached with respect to power extraction:

1) The measured peak open circuit voltage was $V_{\text{oc}} = uBh \sim 10$ V, yielding an effective burned gas velocity of 660 m/s.

2) Measured load-line characteristics were linear away from the extreme loading conditions and indicated decreasing internal plasma resistance with increasing magnetic induction.

3) The energy density scaling parameter ranged from 10 to 10^3 J/m^3 as the effective magnetic induction was varied from 0.6 to 4.2 T.

4) Optimal power extraction shifted from a load impedance of 10 Ω, when $v_0 = 0$ V, to 5 Ω, when $v_0 = 100$ V, due to decreasing internal plasma resistance as the effective magnetic induction and Joule dissipation increased.

5) Theoretical predictions for the energy density scaling parameter in reasonable agreement with measurements given the uncertainties in parameter values.

6) By scaling up to a practical size device and limiting the near-electrode potential drop to 10% of the induced Faraday potential, we anticipate a five- to tenfold increase in power-generation performance with respect to our laboratory-scale results.

Acknowledgments

This work was sponsored by the NASA Marshall Space Flight Center under Contract NAS8-97278 to ERC Incorporated; Contract Monitor Tony Robertson. The authors acknowledge contributive technical discussions with V. A. Bityurin, Head of MHD Division/Coordinator of International Programs, Institute of High Temperatures, Russian Academy of Sciences, Moscow; and with Y. C. L. Susan Wu, President and CEO of ERC Incorporated.

References

[1]Bussing, T., and Pappas, G., "Pulse Detonation Engine Theory and Concepts," *Developments in High-Speed-Vehicle Propulsion Systems*, edited by S. N. B. Murthy and E. T. Curran, Vol. 165, Progress in Astronautics and Aeronautics, AIAA, Reston, VA, 1997, pp. 421–472.

[2]Lynch, E. D., and Edelman, R. B., "Analysis of the Pulse Detonation Wave Engine," *Developments in High-Speed-Vehicle Propulsion Systems*, edited by S. N. B. Murthy and E. T. Curran, Vol. 165, Progress in Astronautics and Aeronautics, AIAA, Reston, VA, 1997, pp. 473–516.

[3]*Pulse-Detonation Engine (PDE) Workshop*, 10th ONR Propulsion Meeting, Office of Naval Research, Energy Conversion—Propulsion Program, Naval Post Graduate School, Monterey, CA, Oct. 1997.

[4]Lineberry, J. T., Litchford, R. J., Lin, B.-C., Wu, Y. C. L., Bityurin, V. A., Veefkind, A., and Holten, A. P. C., "Results of T-Layer MHD Studies," *Proceedings of the 12th International Conference on MHD Electrical Power Generation*, Vol. 1, 1996 (Paper III.20).

[5]Litchford, R. J., Thompson, B. R., Lin, B.-C., and Lineberry, J. T., "High-Temperature Current Layer MHD Power Extraction Experiments," AIAA Paper 97-2397, June 1997.

[6]Jimerin, D. G., Mironov, E. A., and Popov, V. A., "MHD Energy Conversion Using Detonation Conditions," *Proceedings of the 12th Symposium on Engineering Aspects of MHD*, Argonne National Lab., Argonne, IL, 1972, pp. II.4.1– II.4.7.

[7]Matsui, H., and Lee, J. H., "On the Measure of the Relative Detonation Hazards of Gaseous Fuel-Oxygen and Air Mixtures," *Proceedings of the 17th International Symposium on Combustion*, The Combustion Inst., Pittsburgh, PA, 1978, pp. 1269–1280.

[8]Self, S. A., and Kruger, C. H., "Diagnostic Methods in Combustion MHD Flows," *Journal of Energy*, Vol. 1, No. 1, 1977, pp. 25–43.

[9]Wu, Y. C. L., "Performance Theory of Diagonal Conducting Wall MHD Generators," *AIAA Journal*, Vol. 14, No. 10, 1976, pp. 1362–1368.

[10]Gordon, S., and McBride, B. J., "Computer Program for Calculation of Complex Chemical Equilibrium Compositions, Rocket Performance, Incident and Reflected Shocks, and Chapman-Jouguet Detonations," NASA SP-273, 1971.

[11]Glassman, I., *Combustion*, 2nd ed., Academic, Orlando, FL, 1987, p. 222.

[12]Kistiakowsky, G. B., and Mangelsdorf, P. C., "Gaseous Detonations. VIII. Two Stage Detonations in Acetylene-Oxygen Mixtures," *Journal of Chemical Physics*, Vol. 25, No. 3, 1956, pp. 516–519.

[13]Cher, M., and Kistiakowsky, G. B., "Gaseous Detonations. XI. Double Waves," *Journal of Chemical Physics*, Vol. 29, No. 3, 1958, pp. 506–511.

[14]Basu, S., "Ionization in Seeded Detonation Waves," *Physics of Fluids*, Vol. 3, No. 3, 1960, pp. 456–463.

[15]Frost, L. S., "Conductivity of Seeded Atmospheric Pressure Plasma," *Journal of Applied Physics*, Vol. 32, No. 10, 1961, pp. 2029–2039.